# We are IntechOpen, the world's leading publisher of Open Access books Built by scientists, for scientists

**4,800**
Open access books available

**122,000**
International authors and editors

**135M**
Downloads

Our authors are among the

**154**
Countries delivered to

**TOP 1%**
most cited scientists

**12.2%**
Contributors from top 500 universities

CLARIVATE ANALYTICS BOOK CITATION INDEX INDEXED

WEB OF SCIENCE™

Selection of our books indexed in the Book Citation Index in Web of Science™ Core Collection (BKCI)

## Interested in publishing with us?
## Contact book.department@intechopen.com

Numbers displayed above are based on latest data collected.
For more information visit www.intechopen.com

21

# Study and Application of Microwave Active Circuits with Negative Group Delay

Blaise Ravelo, André Pérennec and Marc Le Roy
*UEB France, University of Brest,*
*Lab-STICC, UMR CNRS 3192,*
*France*

## 1. Introduction

Since the early of 1970s, the interpretation of the negative group delay (NGD) phenomenon has attracted considerable attention by numerous scientists and physicists (Garrett & McGumber, 1970; Chu & Wong, 1982; Chiao et al., 1996; Mitchell & Chiao, 1997 and 1998; Wang et al., 2000). Several research papers devoted to the confirmation of its existence, in particular in electronic and microwave domains, have been published (Lucyszyn et al., 1993; Broomfield & Everard, 2000; Eleftheriades et al., 2003; Siddiqui et al., 2005; Munday & Henderson, 2004; Nakanishi et al., 2002; Kitano et al., 2003; Ravelo et al., 2007a and 2008a). In these papers, both theoretical and experimental verifications were performed. The NGD demonstrators that exhibit NGD or negative group velocity were based either on passive resonant circuits (Lucyszyn et al., 1993; Broomfield & Everard, 2000; Eleftheriades et al., 2003; Siddiqui et al., 2005) or on active ones (Chiao et al., 1996; Munday & Henderson, 2004; Nakanishi et al., 2002; Kitano et al., 2003). In practice, it was found that the investigated NGD passive circuits proved to be systematically accompanied with losses sometimes greater than 10 dB. While the active ones which use essentially classical operational amplifiers in feedback with R, L and C passive network were limited at only some MHz. Through experiments with these electronic active circuits, it was pointed out (Mitchell & Chiao, 1997 and 1998; Eleftheriades et al., 2003; Kitano et al., 2003) that the apparition of this counterintuitive phenomenon is not at odds with the causality principle. These limitations, i.e. losses and/or restriction on the frequency range drove us to develop the new NGD cell presented in Fig. 1 (Ravelo, Pérennec and Le Roy, 2007a, 2007b, 2007c, 2008a and 2008b).

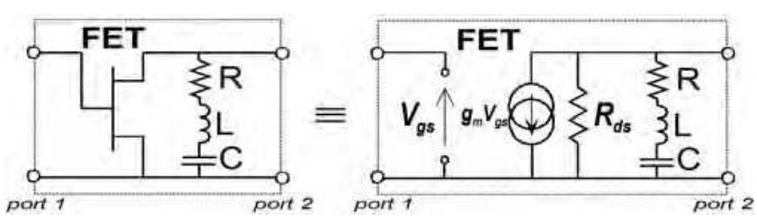


Fig. 1. NGD active cell and its low-frequency model; $g_m$: transconductance and $R_{ds}$: drain-source resistor.

This NGD active cell is composed of a field effect transistor (FET) terminated with a shunt RLC series network. We remark that this cell corresponds typically to the topology of a classical resistive amplifier, but here, focus is only on the generation of the NGD function together with gain. In this way, we recently demonstrated (Ravelo et al., 2007a, 2007b) that the group delay of this NGD cell is always negative at its resonance frequency, $\omega_0 = 1/\sqrt{LC}$. Furthermore, as FETs operating in different frequency ranges are available, the cell is potentially able to operate at microwave wavelengths and over broad bandwidths (Ravelo et al., 2007b). The *a priori* limitations rely on the operating frequency band of the lumped RLC components. By definition, the group delay is given by the opposite of the transmission phase, $\varphi(\omega) = \angle S_{21}(j\omega)$ derivative with respect to the angular frequency, $\omega$:

$$\tau(\omega) = \frac{-\partial \angle S_{21}(j\omega)}{\partial \omega}. \tag{1}$$

Analytical demonstrations and frequency measurements had previously allowed us to state that, in addition to NGD, this active cell can generate amplification with a good access matching. The present chapter is organized in two main sections. The fundamental theory permitting the synthesis of this NGD cell is developed in details in Section 2. Then, through a time domain study based on a Gaussian wave pulse response, the physical meaning of this phenomenon at microwave wavelengths is provided (Ravelo, 2008). From a second effect caused by the gain shape of the NGD active cell shown in Fig. 1, an easy method to realize pulse compression (PC) is also developed and examined. To illustrate the relevance and highlight the benefits of this innovative NGD topology, Section 3 deals with a new concept of frequency-independent active phase shifter (PS) used in recent applications (Ravelo et al., 2008b). This NGD PS is mainly composed of a positive group delay device set in cascade with a negative one of similar absolute value. To validate this innovative PS principle, a hybrid planar prototype was fabricated and tested. The measurements proved to well-correlate to the simulations and showed a phase flatness less than ±10° over a relative frequency band of 100%. Further to the use of two NGD cells, the results of the simulations run with a second PS showed an improvement of the relative constant-phase bandwidth up to about 125 %. These innovative PSs were also used to design and investigate a broadband active balun (Ravelo et al., 2007c). Finally, applications of this microwave NGD active device in telecommunication equipments are proposed, and further improvements are discussed.

## 2. Theoretical and experimental study of the proposed NGD active topology

This Section deals with the analytical and experimental studies of the NGD active cell schematized in Fig. 1. After a brief recall of the S-parameters analysis, the synthesis relations appropriated to this cell are given in Subsection 2.1. Then, Subsection 2.2 is focused on the time-domain response of this cell in the case-study of a Gaussian input-wave pulse; the basic theory evidencing the associated pulse compression phenomenon is proposed. Subsection 2.3 is devoted to the description of experimental results obtained in both frequency- and time-domains; explanations about the process in use to design the NGD active device under test are also provided.

### 2.1 S-parameters analysis and synthesis relations

As established in Ravelo et al., 2007a and 2007b, by using the low-frequency classical model of a FET, the scattering matrix of the ideal NGD cell presented in Fig. 1 is expressed as:

$$S_{11}(j\omega) = 1\,, \tag{2}$$

$$S_{12}(j\omega) = 0\,, \tag{3}$$

$$S_{21}(j\omega) = \frac{-2ZZ_0 g_m R_{ds}}{[Z_0 R_{ds} + Z(Z_0 + R_{ds})]}, \tag{4}$$

$$S_{22}(j\omega) = \frac{ZR_{ds} - Z_0(Z + R_{ds})}{Z_0 R_{ds} + Z(Z_0 + R_{ds})}, \tag{5}$$

where

$$Z = R + j[L\omega - 1/(C\omega)]\,. \tag{6}$$

$Z_0$ is the port reference impedance, usually 50Ω. At the resonance angular frequency, $\omega = \omega_0 = 1/\sqrt{LC}$, one gets $Z = R$, and then equations (4) and (5) become:

$$|S_{21}(\omega_0)| = \frac{2RZ_0 g_m R_{ds}}{[Z_0 R_{ds} + R(Z_0 + R_{ds})]}, \tag{7}$$

$$|S_{22}(\omega_0)| = \frac{|RR_{ds} - Z_0(R + R_{ds})|}{|Z_0 R_{ds} + R(Z_0 + R_{ds})|}. \tag{8}$$

At this frequency, it was demonstrated (Ravelo et al., 2007a and 2007b) that the group delay expressed in equation (1) is always negative:

$$\tau(\omega_0) = \frac{-2LZ_0 R_{ds}}{R[RR_{ds} + Z_0(R + R_{ds})]}\,. \tag{9}$$

The synthesis relations relative to the NGD cell are extracted from equations (8) and (9). As shown hereafter, they depend on the given gain magnitude and group delay ($S_{21}$ and $\tau_0$, respectively) at the resonance, $\omega_0$:

$$R = \frac{S_{21} Z_0 R_{ds}}{[2g_m Z_0 R_{ds} - S_{21}(Z_0 + R_{ds})]}, \tag{10}$$

$$L = \frac{-\tau_0 R[RR_{ds} + Z_0(R + R_{ds})]}{(2Z_0 R_{ds})}\,. \tag{11}$$

Then, the $C$ synthesis relation is deduced from the expression of the resonance angular frequency:

$$C = \frac{1}{(L\omega_0^2)}\,. \tag{12}$$

As previously mentioned, in addition to this NGD property, this circuit allows compression of the width of a modulated Gaussian pulse centred at $\omega_0$. The compression theory will be developed in the next section.

### 2.2 Study of the Gaussian-pulse response: evidence of time domain advance and pulse compression (PC)

Fig. 2 illustrates the configuration under consideration in the time-domain study. It consists of a black box of the NGD circuit S-parameters excited by a sine carrier, $f_0 = \omega_0/(2\pi)$, modulated by a Gaussian pulse. In order to evidence the principle of this NGD phenomenon, let us consider the input signal expressed as:

$$x(t) = e^{-\frac{(t-t_0)^2}{2\Delta T_x^2}} \times e^{j\omega_0 t} . \tag{13}$$

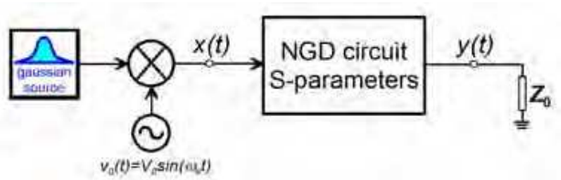


Fig. 2. Block diagram of the understudied configuration considered in time-domain ($Z_0$ = 50 Ω).

$\Delta T_x$ is the standard deviation (half width at $1/e$ of the maximal input value) and $t_0$ is the central time of the Gaussian pulse. It ensues that the Fourier transform of such a signal is defined as:

$$X(j\omega) = \Delta T_x \sqrt{2\pi} e^{-0.5\Delta T_x^2(\omega-\omega_0)^2 - j(\omega-\omega_0)t_0} . \tag{14}$$

According to the signal processing theory, this function is also Gaussian, and its angular frequency standard deviation is:

$$\Delta\omega_x = 1/\Delta T_x . \tag{15}$$

It means that the pulse compression in time domain involves a pulse expansion in frequency domain and vice versa. Then, the standard deviation of the Gaussian output is compared, at first theoretically, with the input one through the transmittance, $H(j\omega)$. To highlight this analytical approach, let us consider the black box system shown in Fig. 2. As its transfer function, $H(j\omega)$, is excited by $X(j\omega)$, the output Fourier transform is:

$$Y(j\omega) = H(j\omega)X(j\omega) = e^{\ln|H(j\omega)| + jArg[H(j\omega)]}X(j\omega) . \tag{16}$$

A simplified and approximated analytical study is proposed hereafter in order to analyze the behaviour of this output. First, we consider the Taylor series expansion of the magnitude, $ln|H(j\omega)|$, around the resonant angular frequency, $\omega_0$:

$$\ln\left|H_a(j\omega)\right| \approx \ln\left|H(\omega_0)\right| + \frac{H'(\omega_0)}{H(\omega_0)}(\omega-\omega_0) + \frac{H''(\omega_0)}{2H(\omega_0)}(\omega-\omega_0)^2 + O[(\omega-\omega_0)^3], \quad (17)$$

where $H'(\omega_0)$ and $H''(\omega_0)$ are respectively the first- and second-order derivatives of $|H(j\omega)|$ with respect to $\omega$. Then, application of the same procedure to the transmission phase, $\varphi(\omega) = \angle S_{21}(j\omega)$ leads to the following approximated expression:

$$\begin{aligned}\varphi_a(\omega) &\approx \varphi(\omega_0) + \varphi'(\omega_0)(\omega-\omega_0) + 0.5\varphi''(\omega_0)(\omega-\omega_0)^2 + O[(\omega-\omega_0)^3] \\ &= \varphi(\omega_0) - \tau(\omega_0)(\omega-\omega_0) - 0.5\tau'(\omega_0)(\omega-\omega_0)^2 + O[(\omega-\omega_0)^3]\end{aligned}. \quad (18)$$

At resonance, $\varphi(\omega_0) = 0$, and in the vicinity of $\omega_0$, one gets $\tau'(\omega_0) \approx 0$, this implies that:

$$\varphi_a(\omega) \approx -\tau(\omega_0)(\omega-\omega_0) + O[(\omega-\omega_0)^3]. \quad (19)$$

One should note that the terms of higher order can be ignored if the input signal bandwidth is small enough compared to the NGD bandwidth. As this phase response is relatively linear, the $Y(j\omega)$-magnitude is unaffected. So, the output modulus can be written as:

$$\left|Y(j\omega)\right| \approx \left|H(\omega_0)\right| e^{\frac{H'(\omega_0)}{H(\omega_0)}(\omega-\omega_0)+\frac{H''(\omega_0)}{2H(\omega_0)}(\omega-\omega_0)^2} \times \left|X(j\omega)\right|. \quad (20)$$

By substituting for $X(j\omega)$ from equation (14) in equation (20), one gets:

$$\left|Y(j\omega)\right| \approx \left|H(\omega_0)\right| \Delta T_x \sqrt{2\pi}\, e^{\frac{H'(\omega_0)}{H(\omega_0)}(\omega-\omega_0)-\frac{1}{2}\left[\Delta T_x^2 - \frac{H''(\omega_0)}{H(\omega_0)}\right](\omega-\omega_0)^2}. \quad (21)$$

The magnitude of the insertion gain is defined as:

$$\left|H(j\omega)\right| = \frac{2Z_0 g_m R_{ds}\sqrt{R^2 + [(L\omega - 1/(C\omega)]^2}}{\sqrt{[Z_0 R_{ds} + R(Z_0 + R_{ds})]^2 + (Z_0 + R_{ds})^2[(L\omega - 1/(C\omega)]^2}}. \quad (22)$$

At $\omega_0$, this expression becomes:

$$\left|H(\omega_0)\right| = \frac{2g_m R_{ds} Z_0 R}{R_{ds}R + Z_0(R + R_{ds})}, \quad (23)$$

and the first- and second-order derivatives are expressed as follows:

$$H'(\omega_0) = \left.\frac{\partial\left|H(j\omega)\right|}{\partial\omega}\right|_{\omega=\omega_0} = 0, \quad (24)$$

$$\left|H(\omega_0)\right|'' = \left.\frac{\partial^2\left|H(j\omega)\right|}{\partial\omega^2}\right|_{\omega=\omega_0} = \frac{8g_m R_{ds}^2 Z_0^2 L^2\left[R_{ds}Z_0 + 2R(Z_0+R_{ds})\right]}{R\left[R_{ds}R + Z_0(R+R_{ds})\right]^3} > 0\,. \tag{25}$$

It ensues that the output amplitude of equation (21) can be simplified as follows:

$$\left|Y(j\omega)\right| \approx \left|H(\omega_0)\right|\Delta T_x\sqrt{2\pi}e^{-0.5[\Delta T_x^2 - H''(\omega_0)/H(\omega_0)](\omega-\omega_0)^2}\,. \tag{26}$$

In fact, thanks to the second-order expansion expressed in equation (26), the output Fourier transform also behaves as a Gaussian pulse:

$$\left|Y(j\omega)\right| \approx Y_{\max}e^{-(\omega-\omega_0)^2/(2\Delta\omega_y^2)}, \tag{27}$$

of amplitude:

$$Y_{\max} = \frac{2g_m R_{ds}Z_0 R}{R_{ds}R + Z_0(R+R_{ds})}\Delta T_x\sqrt{2\pi}\,. \tag{28}$$

and with an angular frequency standard deviation such as:

$$\Delta\omega_y = \frac{1}{\sqrt{\Delta T_x^2 - H''(\omega_0)/H(\omega_0)}} = \frac{\Delta\omega_x}{\sqrt{1 - H''(\omega_0)/[H(\omega_0)\Delta T_x^2]}}\,. \tag{29}$$

Furthermore, the pulse width is expanded in the frequency domain ($\Delta\omega_x > \Delta\omega_y$). In the time domain, the approximated output signal inferred from the inverse Fourier transform of equation (26) is written as:

$$y(t) = \frac{\left|H(\omega_0)\right|\Delta T_x}{\sqrt{\Delta T_x^2 - H''(\omega_0)/H(\omega_0)}}e^{-\frac{0.5[t-t_0-\tau(\omega_0)]^2}{\Delta T_x^2 - H''(\omega_0)/H(\omega_0)}} \times e^{j\omega_0 t}\,. \tag{31}$$

It can be seen that this output behaves as a modulated Gaussian that exhibits a time advance whenever $\tau(\omega_0) < 0$; moreover, the standard deviation is expressed as:

$$\Delta T_y = \sqrt{\Delta T_x^2 - \frac{4L^2 R_{ds}Z_0\left[R_{ds}Z_0 + 2R(Z_0+R_{ds})\right]}{R^2\left[R_{ds}R + Z_0(R+R_{ds})\right]^2}}\,. \tag{32}$$

This is obvisously an approximated expression because it comes from a first-order limited expansion of equation (17). Due to the intrinsic behaviour of linear devices, the higher order terms ensure that $\Delta T_y$ cannot tend to zero.

Hence, in practice, equation (32) corresponds to a compression of the pulse width in the time domain. Furthermore, compared to the input pulse, $x(t)$, the output one, $y(t)$ is amplified by the quantity:

$$\alpha = \left|H(\omega_0)\right|.\Delta T_x / \Delta T_y \,. \tag{33}$$

As reported by Cao and co-workers (2003), if $\Delta T_x$ is getting closer to $\Delta T_{xmin}$, it goes along with a significant PC.

- *Remarks on the PC phenomenon*: Various PC techniques have been developed at optical- and microwave-wavelengths in order to convert a long-duration pulse into a shorter one. One should note that the principles and methods proposed in the literature depend on whether the applications under study are dedicated to low or high power (Gaponov-Grekhov & Granatstein, 1994; Thumm & Kasparek, 2002). For example, PC was investigated in ultra-fast laser systems (Li et al., 2005), then its use has become more and more common thanks to the development of chirped pulse amplification (Arbore, 1997; Wang & Yao; 2008a and 2008b). The next step was the compression of a pulse in a Mach-Zehnder-interferometer geometry achieved by passing a broadband ultra-short pulse through two chirped fibre Bragg gratings with different chirp rates (Zeitouny et al., 2005). In radar and communication systems, PC has been used to enhance the range resolution. In order to elevate microwave power, investigations by several authors have been focused on a microwave pulse compressor based on a passive resonant cavity (Burt et al., 2005; Baum, 2006). The prerequisites are that the compressor cavity must present a high Q-factor; in addition, the constituting waveguides should operate with an oversized mode of the field in order to increase the power strength, and the power microwave sources should be narrow-band. This set of requirements is met by quasi-optical cavities, particularly by the ring-shaped multi-mirror ones, where the energy is sent to the cavity via corrugated mirror (Kuzikov et al., 2004). But, as in practice the implementation of such a technique is usually very complex and at high cost, a new and much simpler PC technique based on the use of NGD structure was recently proposed (Cao et al., 2003) by using a classical operational amplifier. Though application of this technique to rather low power devices remains possible, one should be aware that it is intrinsically restricted to low frequencies.

  The PC method proposed here is close to this latter study, but it is able to operate in the microwave frequency range.

All of these predictions from theory have to be experimentally verified; but prior to the discussion of the corresponding experimental results, it is worth describing the design process of the NGD devices under study.

### 2.3 Experimental study

***(a) Design process***:

The flow chart displayed in Fig. 3 lists the sequence of actions to be followed to design NGD active circuits. One should note that the proposed process is well-suited to the use of classical circuit simulator/designer software such as, for example, ADS software from *Agilent™*.

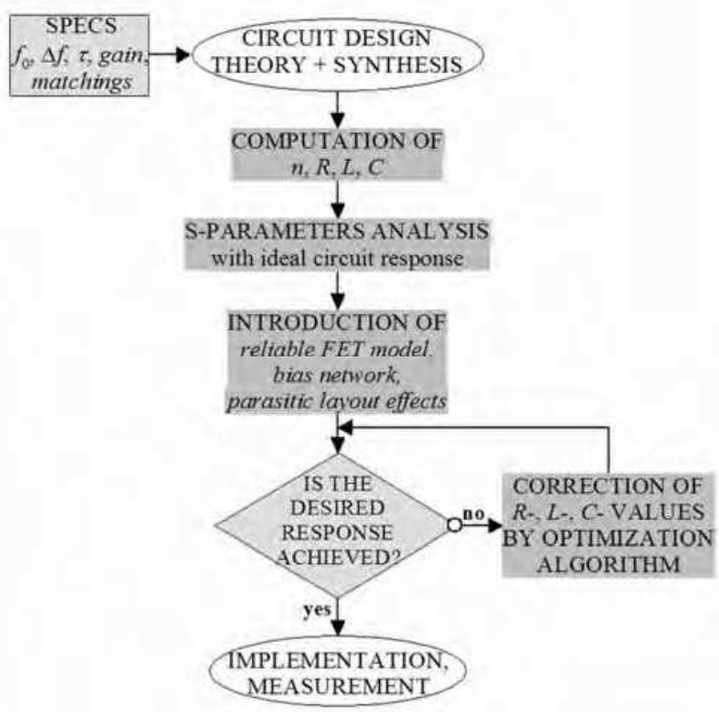


Fig. 3. Flow chart of the NGD-device design process (*n* is the number of NGD cells).

The technique used to design these devices is similar to the one developed in the case of classical microwave devices (filter, amplifier, coupler …). During the synthesis of the circuit under study, focus is on the NGD level and the gain value at the centre frequency of the operating band. If the FET characteristics, $g_m$ and $R_{ds}$, are known, the synthesis relations (10), (11) and (12) introduced in section 2.1 can be used to calculate the values of the RLC resonant-network components included in the NGD active cell. For a more realistic approach, it is worth taking into account a reliable (complete linear or non-linear) model of the employed FET including bias network, the effects of distributed interconnect lines and the actual manufacturing details. The combined use of a circuit simulator with an electromagnetic simulation tool such as Momentum from *ADS*™ provides more accurate responses. To get acceptable final responses, slight optimizations may be needed prior to implementation and measurements.

***(b) Implementation of the proposed prototype***: To check for the validity of the aforementioned theoretical predictions on NGD and PC, a proof-of-principle device consisting of an NGD active circuit with three resonant cells (Figs. 4) was designed, fabricated and tested. One should note that the measurement instruments available within our laboratory to evidence both the NGD and PC phenomena had to be considered prior to the selection of the operating band.

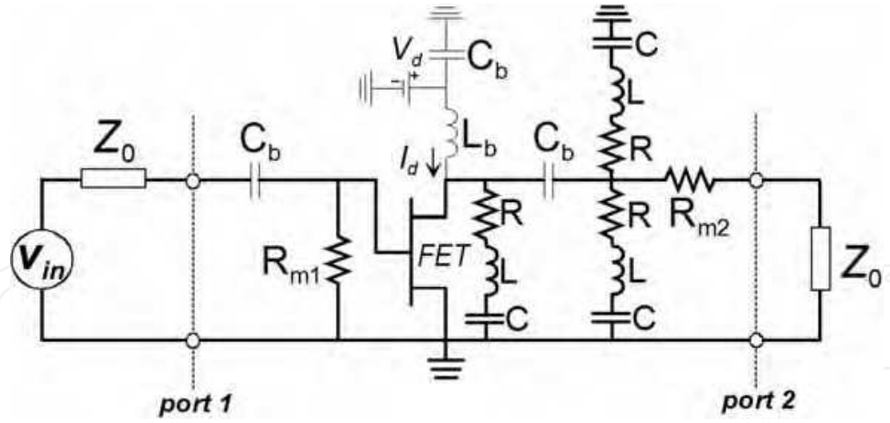


(a)

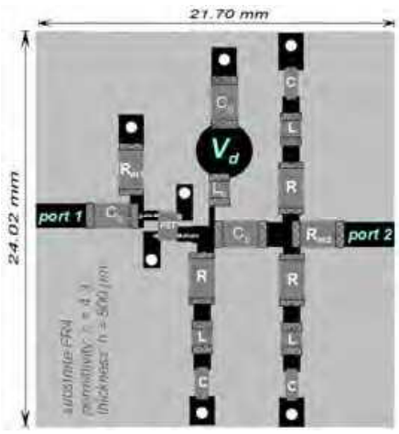


(b)


(c)

Fig. 4. Fabricated NGD active device: (a) Schematic (bias circuit in thin line), FET (ATF-34143 biased at $V_d$ = 2V, $I_d$ = 100 mA), $R_{m1}$ = 82 Ω, $R_{m2}$ = 22 Ω, $R$ = 18 Ω, $L$ = 51 nH, $C$ = 0.5 pF, $C_b$ = 1 nF, $L_b$ = 220 nH; (b) layout; (c) photograph.

As pictured in Figs. 4(b) and 4(c), it is a hybrid planar circuit fabricated with surface mount chip components and printed on an FR4 substrate with relative permittivity, $\varepsilon_r$ = 4.3 and thickness, $h$ = 800 µm. The active element is a PHEMT FET (ATF-34143) mounted in plastic package from *Avago Technology*™. The implemented circuit is biased through an RF-choke inductance (biasing point: $V_d$ = 2V, $I_d$ = 100 mA) and cascaded with three RLC series resonant cells in shunt. These three cells were used in order to evidence, with the components at our disposal, both the compression and the NGD effects. The transconductance and the drain-source resistance, $g_m$ = 226 mS and $R_{ds}$ = 27 Ω, respectively, were extracted from the S-parameters of the FET non linear model provided by the manufacturer and further used to synthesize the NGD-cell component values. Then, these values were optimized through electromagnetic and schematic co-simulations carried out with *Momentum* software from *ADS*™.

***(c) Results of frequency-domain measurements***: Figs 5(a) and 5(b) describe the results of the frequency measurements made with an *EB364A Agilent Vector Network Analyzer*.

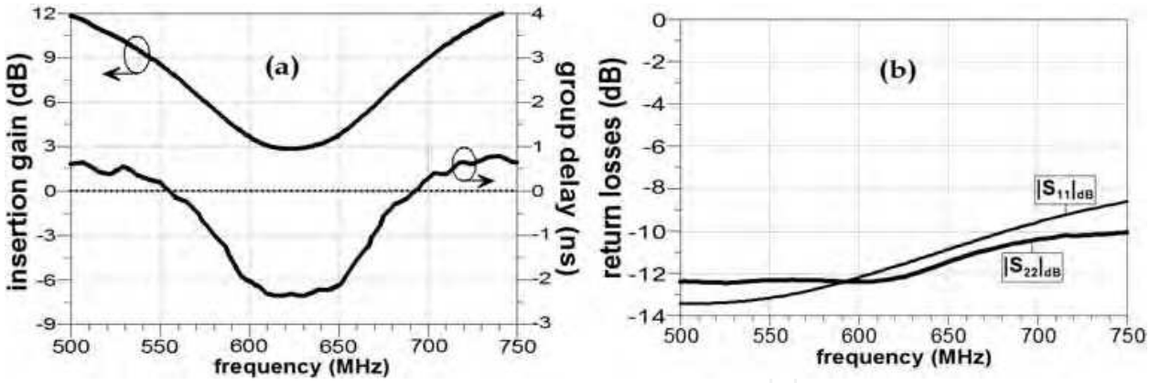


Fig. 5. Measured results: (a) insertion gain/group delay, and (b) return losses.

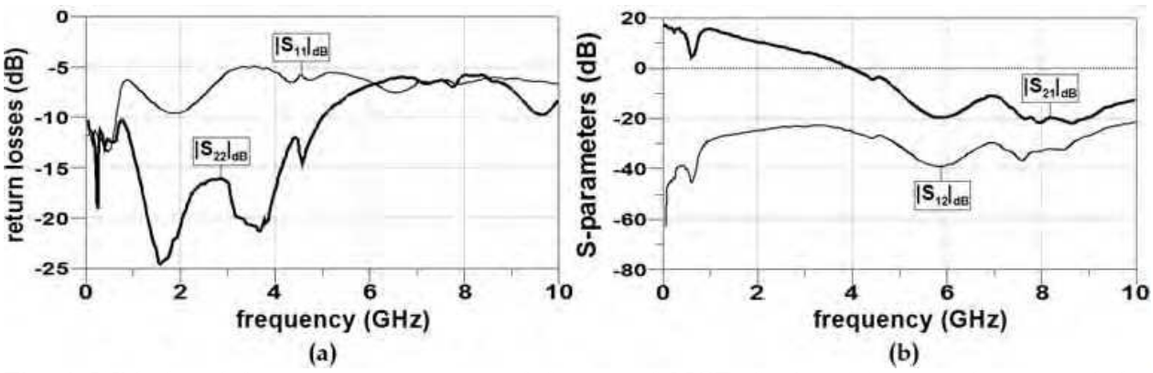


Fig. 6. Wide band frequency responses of the tested NGD device: (a) return losses and (b) $S_{21}$-parameter and isolation loss.

Fig. 5(a) shows that, in a frequency band of about 135 MHz in width and centred around 622 MHz, the gain and the group delay are better than 2 dB and lower than –2 ns, respectively. In the same frequency band, Fig. 5(b) indicates that the matching level for this NGD device is better than –9 dB. Furthermore, the necessary, but not sufficient, condition for stability is also confirmed by measurements over a wider band (Fig. 6(a)) with return losses $|S_{11}|$dB and $|S_{22}|$dB better than 5 dB. In addition, Fig. 6(b) shows that the gain, $|S_{21}|_{dB}$, and isolation loss, $|S_{12}|_{dB}$, exhibited by this NGD device are, respectively, lower than 18 dB and -20 dB over the range from DC to 10 GHz.
At this stage, for a more comprehensive study of NGD-induced effects, let us continue with the time-domain experimental characterization.

***(d) Time-domain measurements***: In order to allow operation in the specified frequency band and to meet the conditions stated in section 2.2, time-domain measurements were made for a Gaussian wave pulse (8.4 ns as standard deviation) modulating a 622 MHz carrier. This signal was provided by a vector signal generator *Rhode & Schwarz SMJ 100A* and measured with a *2 Gs/s LeCroy* Digital Oscilloscope.

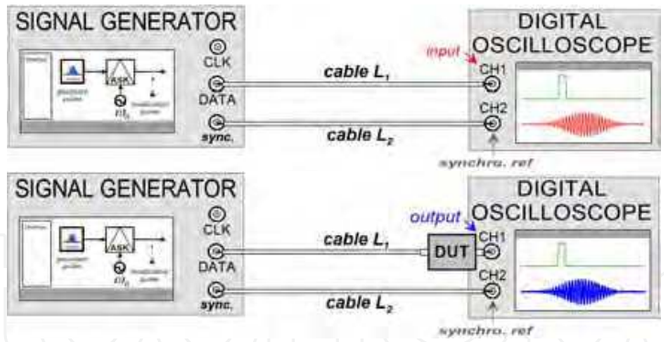


**(a)**

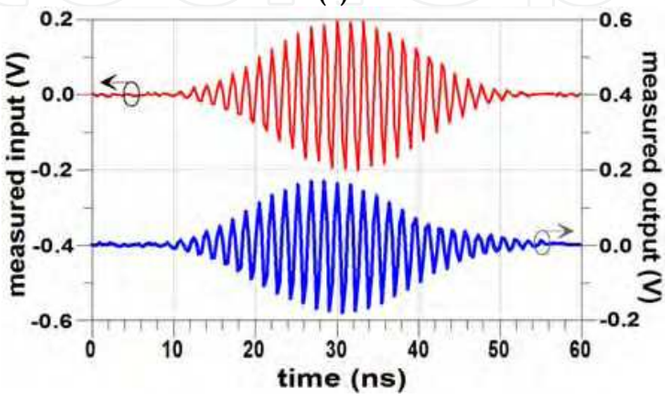


**(b)**

Fig. 7(a). Experimental setup diagram and (b) response by the circuit shown in Fig. 4 in the case of a 622-MHz carrier modulated by a Gaussian input (about 8.4 ns as standard deviation).

Figs. 7 show that the measured output behaves as a Gaussian pulse and is slightly compressed because of the gain shape around the resonance as previously demonstrated. As explained in Fig. 7(a), to avoid cable and connector influences, the first signal to be recorded was the input one. Then it was replaced by the output one (connected to CH1). In both cases, the synchronization reference signal was the same (connected to CH2). Then, the recorded input modulated pulse and NGD DUT output (see thin red line and thick blue one, respectively, in Fig. 7(b)) were resynchronized from the same reference signal (CH2 channel). It is interesting to note that the input-pulse width was the shortest one that the signal generator in use could generate. These results indicate that the pulse width needs to be smaller to better evidence the effects by NGD- and compression. For that reason, we propose the following simulations.

***(e) Time domain simulations***: These transient simulations were run on using the S-parameters issued from measurements. The input pulse was Gaussian and such that its standard deviation was equal to $\Delta T_x \approx 4.0$ ns; it modulated a 622 MHz sine carrier, corresponding to the centre frequency of the NGD circuit response (see Figs. 2 and 5(a)). In the frequency domain, it gives a Gaussian pulse (dotted line in Fig. 8(a)) with $\Delta f_x \approx 40$ MHz as frequency standard deviation. As shown in Fig. 8(a), the resulting output spectrum (in blue solid line) can be approximated to a Gaussian pulse with a frequency standard deviation of about $\Delta f_y \approx 50$ MHz (or $\Delta T_x \approx 3.3$ ns). In frequency domain, the output pulse

width is thus expanded of about 125% and amplified of about 3.86 dB with respect to the input pulse one.

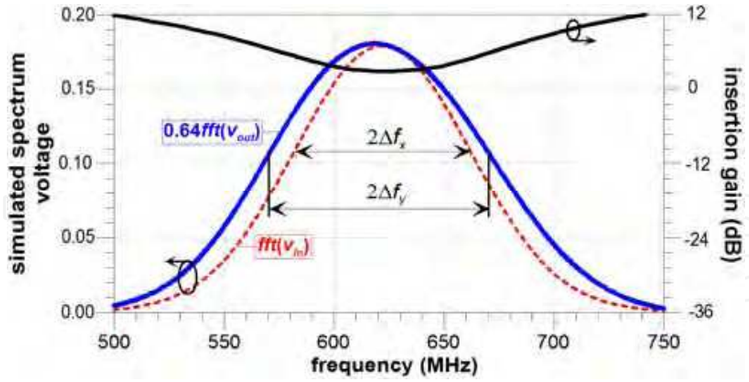


Fig. 8(a). Simulated spectra of the input and output voltage (Fourier transforms) issued from simulations run on using the measured S-parameters.

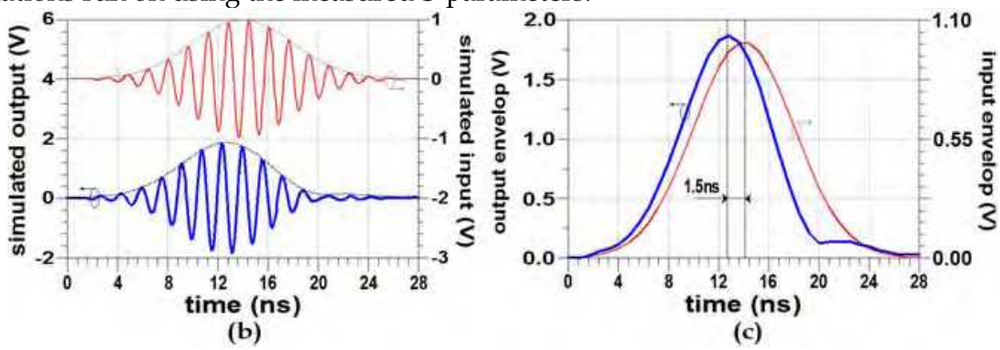


Fig. 8. Simulated results run on using the measured S-parameters: (b) transient- and (c) envelop-voltages.

Figs. 8(b) and 8(c) show that the PC is about 80% in time-domain; moreover, a comparison of the maxima of the input and output pulse envelopes (Fig. 8c) demonstrates that the time advance induced by the NGD effect is about 1.5 ns. As reported in (Ravelo et al., 2008a) further to the implementation of a two-stage NGD circuit, the NGD value was higher over a wide bandwidth centred at about 1 GHz. This means that the pulse-peak advance and PC values can be both improved when several NGD stages are used.
As experiments led, as expected, to the simultaneous generation of both NGD and gain over a rather wide bandwidth at microwave frequencies, it is now worth focusing on the design of microwave devices through use of these properties.

## 3. Design of frequency-independent phase shifter (PS) and -balun based on NGD active circuits

We recently reported on the use of such NGD active circuits in the design of a frequency-independent phase shifter (PS) (Ravelo, 2008). Let us, at first, recall the underlying innovative and simple fundamental principle. Then, a preliminary study on the influence of RLC-element variations on the PS-responses will be detailed and discussed. The design of a proof-of-concept PS through use of a single stage of NGD active cell will be described prior

to the analysis and discussion of the experimental results. Then, simulations of a two-stage NGD PS will be reported to illustrate both the possibility of achieving broadband of constant phase and the relative insensitivity of the response versus the component tolerances. The last part will deal with the design and simulations of a broadband active balun based on the use of these NGD PSs.

### 3.1 Principle of the proposed frequency-independent PS

Figs. 9(a) and 9(b) illustrate the fundamental principle of this NGD PS. As shown in Fig. 9(a), the block diagram of the NGD PS under study is composed of two devices set in cascade. The former block, e.g. a transmission line (TL), exhibits a constant positive group delay (PGD) and the latter has of course, a negative one (NGD) of equal magnitude in the desired operating frequency band (see Figs 9(b)).

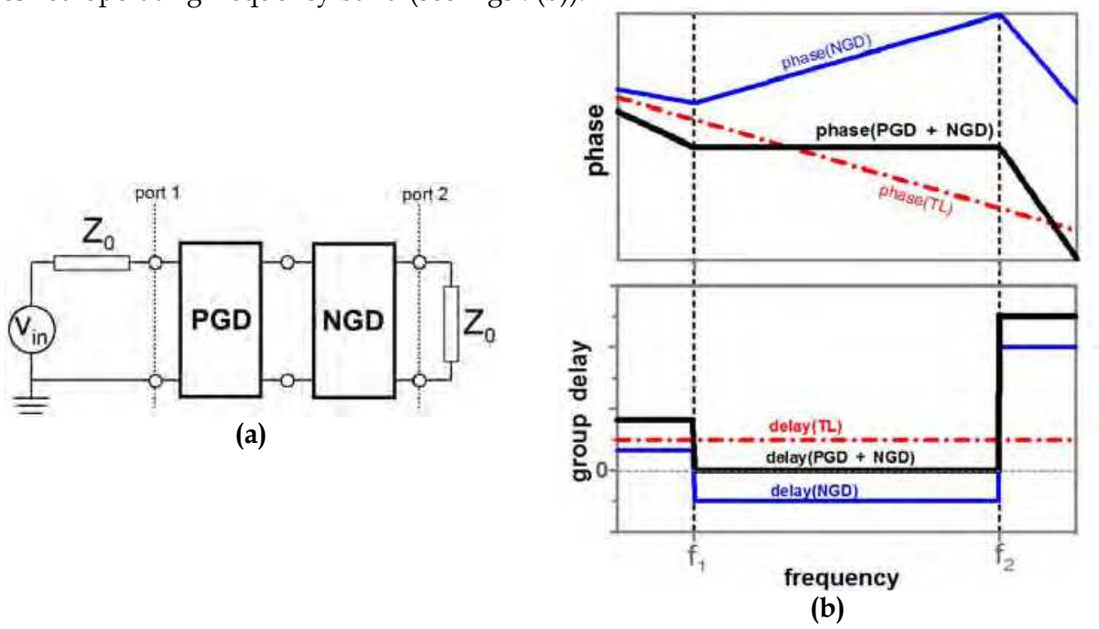


Fig. 9(a). Architecture of the proposed NGD PS and (b) ideal behaviour of the phase and group delay responses ($Z_0$: reference impedance).

In the case of a perfect matching between the PGD- and NGD-blocks and on the condition that the phase slopes of these PGD- and NGD-blocks are alike in absolute value, but of unlike signs, the phase response of the whole circuit will be constant as depicted in Fig. 9(a). It implies that the corresponding group delay, $\tau(\omega) = -\partial\varphi(\omega)/\partial\omega$ is mathematically equal to zero. When denoting by $\tau_p$ and $\tau_n$, the group delays of the considered PGD- and NGD-blocks, respectively, the analytical expressions of their phase responses are:

$$\Phi_p(f) = -2\pi\tau_p(f - f_1) + \Phi_p(f_1), \tag{34}$$

$$\Phi_n(f) = -2\pi\tau_n(f - f_1) + \Phi_n(f_1), \tag{35}$$

As previously argued, in the ideal case of a perfect impedance matching, the total phase response, $\Phi_t$ is merely the sum of $\Phi_p$ and $\Phi_n$. This implies the total phase response:

$$\Phi_t(f) = -2\pi(\tau_n + \tau_p)(f - f_1) + [\Phi_p(f_1) + \Phi_n(f_1)]. \tag{36}$$

Since the operating principle implies that the group delay absolute values are equal ($\tau_p$ = -$\tau_n$), this quantity can be simplified as:

$$\Phi_t(f) = \Phi_p(f_1) + \Phi_n(f_1)\,. \tag{37}$$

The synthesis relations of the proposed PS were previously detailed in Ravelo et al., 2008b. To illustrate and validate the proposed principle, the following section will deal with the design of a proof-of-concept PS and analysis of simulation- and measurement-results.

### 3.2 Designs, simulations and experimental results of frequency independent PSs by using NGD active circuits

A PS prototype with one NGD cell (Fig. 10) was designed on using the NGD cell synthesis relations established in section 2.1 in order to investigate the influence of the RLC component values on the magnitude- and phase-responses of $S_{21}$-parameter. Then, another one-stage NGD PS prototype was fabricated to validate the principle of the PS under study and to assess its performances through measurements. In order to improve the frequency bandwidth of constant phase, a two-stage NGD device was designed through simulations and subjected to a Monte-Carlo sensitivity analysis.

***(a) Study of RLC-element variations***: In this paragraph, the aim is to gain more insight into the evolution of the $S_{21}$-magnitude and -phase behaviours versus the component values. This preliminary sensitivity analysis may serve as an initial study for the design of a reconfigurable PS.

The circuit under study is depicted in Fig. 10, the FET was modelled by its non-linear model; moreover, the biasing network and the interconnect lines were both taken into account in the simulations. As preliminary remark, due to the non-reciprocity of the FET, $S_{11}$ is unaffected by variations of any element of the RLC-network. On the other hand, a significant change of the $R$-value can induce a variation of the $S_{22}$-output return loss.

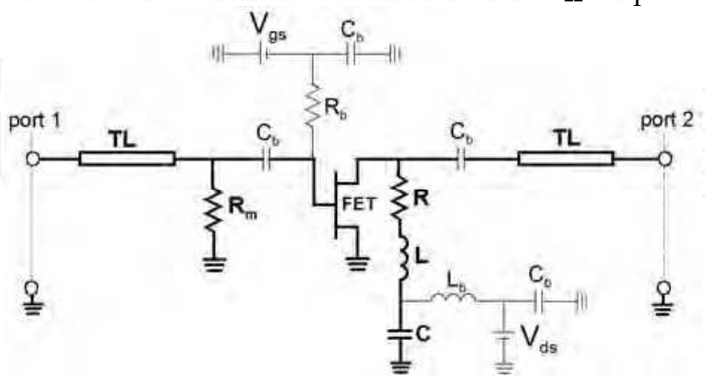


Fig. 10. Detailed schematic of the simulated NGD PS (biasing network in thin line): $R_m$ = 51 Ω, $C_b$ = 22 nF, $L_b$ = 390 nH, $R_b$ = 1 kΩ, FET/EC-2612 ($V_{gs}$ = -0.1 V, $V_{ds}$ = 3 V, $I_{ds}$ = 30 mA) and $TL$ ($w$ = 952 μm, $d$ = 3.7 mm) printed on an FR4 substrate with relative permittivity, $\varepsilon_r$ = 4.3, and thickness, $h$ = 508 μm.

- *Effects of R variations*: Figs. 11(a) and 11(b) show that the gain and flatness are both affected by variations on *R*. *I*ncrease of *R*-value leads to a simultaneous enhancement of the gain value and flatness. Then, the phase slope is affected, but, logically, with no change on the centre frequency of the PS.

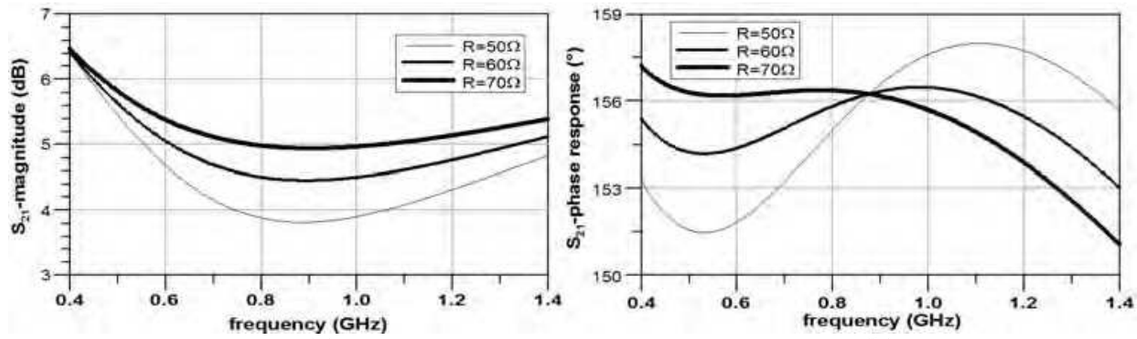


**(a)** **(b)**

Fig. 11. Simulations of the circuit presented in Fig. 10: influence of R-variations on the gain (a), and on the phase (b) when $L$ = 6.2 nH and $C$ = 5 pF.

- *Effects of L variations*: Figs. 12 highlight a shift of the NGD cell resonance frequency ($\omega_0 = 1/\sqrt{LC}$) induced by *L*-variation as well as the shift of the PS centre frequency. In fact, according to equation (9), the modification of the self value affects linearly the group delay, and thus the phase form.

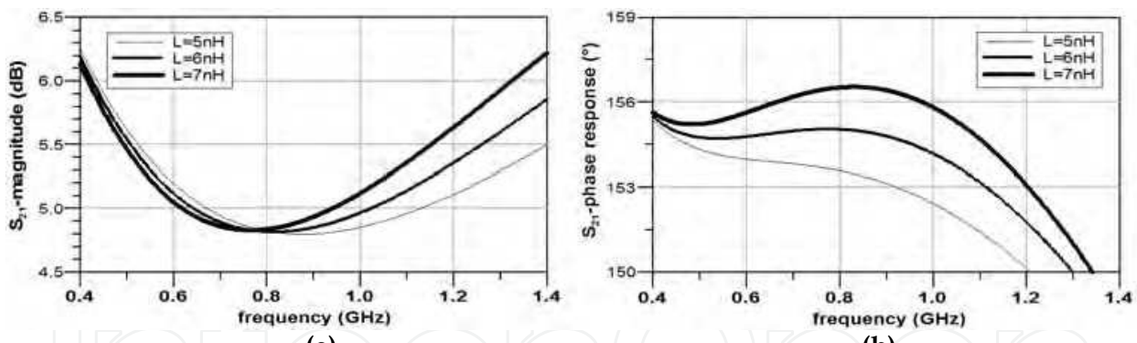


**(a)** **(b)**

Fig. 12. Simulations of the circuit presented in Fig. 10: influence of L-variations on the gain (a) and the phase (b) when $R$ = 68 Ω and $C$ = 5 pF.

- *Effects of C variations*: Contrarily to the two previous cases, Figs. 13 show that the form of the frequency responses (gain and phase) are rather unaffected by *C*-variation. On the other hand, it has a significant impact on both the centre frequency and the constant phase value.

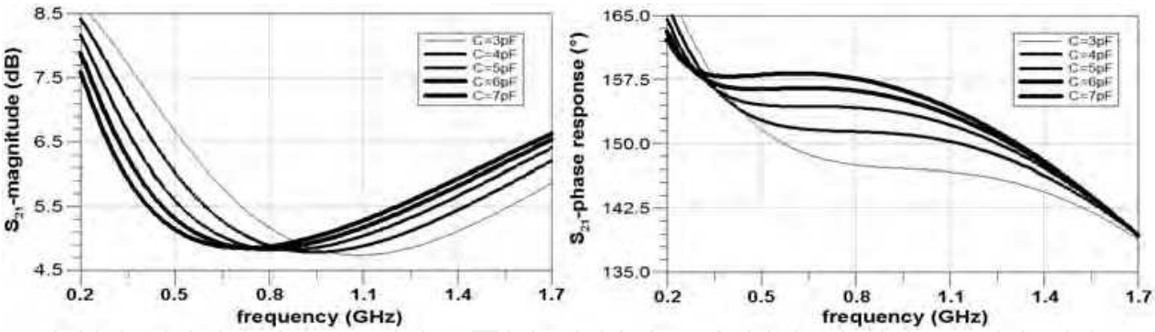


Fig. 13. Simulations of the circuit presented in Fig. 10: influence of C-variation on the gain (a) and the phase (b) when $R$ = 68 Ω and $L$ = 6.2 nH.

***(b) Experimental results of a PS prototype using one NGD cell***:

Fig. 14(a) presents the schematic of the fabricated NGD PS. It relies on the use of a PHEMT FET (EC-2612) manufactured by *Mimix Broadband*™ with characteristics, $g_m$ = 98.14 mS and $R_{ds}$ = 116.8 Ω in inductive bias ($V_{gs}$ = -0.1 V, $V_{ds}$ = 3 V and $I_{ds}$ = 30 mA). For this proof-of-concept circuit, the objective was to reach a constant value of 90° in the operating frequency band. It was voluntarily centred below 2.5 GHz in order to minimize the spurious effects induced by low lumped component values. As indicated by the layout and the photograph respectively pictured in Figs. 14(b) and 14(c), this prototype was implemented in planar hybrid technology printed on an FR4-substrate with permittivity, $\varepsilon_r$ = 4.3 and thickness, $h$ = 508 µm. About the $S_{21}$-transmission phase and the group delay, Fig. 15(a) illustrates the good agreement between the results of simulations and measurements especially from 0.5 to 1.8 GHz. In addition, the phase measurement shows a flatness of about ±5° around 90° from 1.08 to 2.42 GHz. It corresponds to a 76.5% relative bandwidth which is wider than the one obtained by simulation. Moreover, the relative bandwidth increases up to 100% if a ±10° variation around 90° is considered.

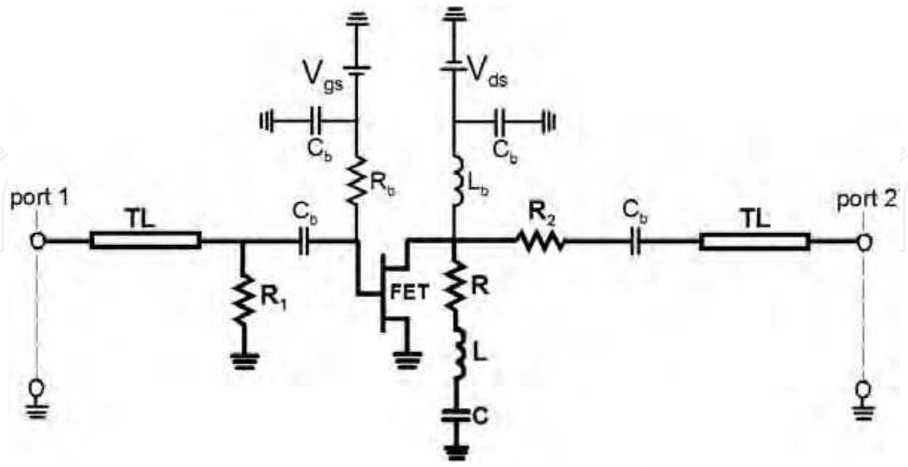


Fig. 14(a): Detailed schematic (biasing network in thin line) of the tested NGD PS : $R_1$ = 51 Ω, $R_2$ = 22 Ω, $R$ = 33 Ω, $L$ = 4.7 nH, $C$ = 1 pF, $C_b$ = 22 µF, $L_b$ = 220 nH, $R_b$ = 1 kΩ, FET (EC-2612 biased at $V_{gs}$ = -0.1 V, $V_{ds}$ = 3 V and $I_{ds}$ = 30 mA) and *TL* ($w$ = 952 µm, $d$ = 6.2 mm).

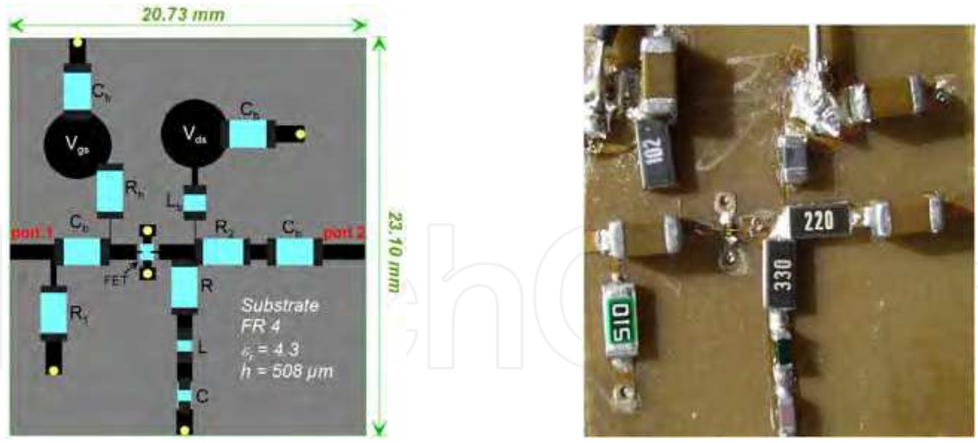


**(b)** **(c)**

Fig. 14. Tested NGD phase shifter: (b) layout and (c) photograph.

Fig. 15(a) shows that the group delay of the PS under test is fairly negative around 1.7 GHz. Furthermore, in the frequency band of concern, its average value is in practice lower than the group delay generated by a passive device of similar physical length such as a classical transmission line. Fig. 15(b) shows that the flatness of $S_{21}$-magnitude is about 4 dB around 0 dB. The difference on the gain level likely comes from the dispersion of the values chosen for the passive components and from the transistor model. In fact, the value of gain obtained by measurement is, on average, 2 dB lower than by simulation one; about the group delay flatness, one should note that the measurement gives a better value than the simulation. Moreover, Fig. 15(c) about the comparison between simulations and measurements of the $S_{11}$ input- and $S_{22}$ output- reflexion coefficients shows that the input and output matching levels are better than -10 dB from 1.1 GHz to 2.0 GHz. Thanks to the non-reciprocity of the transistor in use, the fabricated phase shifter presents an excellent isolation. Moreover, as explained by Fig. 15(c), a significant access-matching margin is obtained up to 4 GHz. But, these results are not sufficient to guarantee PS stability. So, from simulations run with ADS and by using S-probe components, the stability of this PS was analyzed by checking that the magnitude of the input and output reflection coefficients of the FET was kept below one from 1 GHz up to 10 GHz

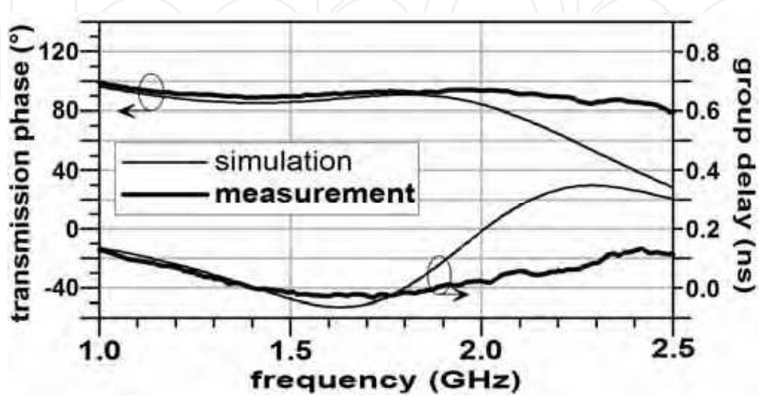


Fig. 15(a). Comparisons of the transmission phase/group delay values obtained by simulations and measurements.

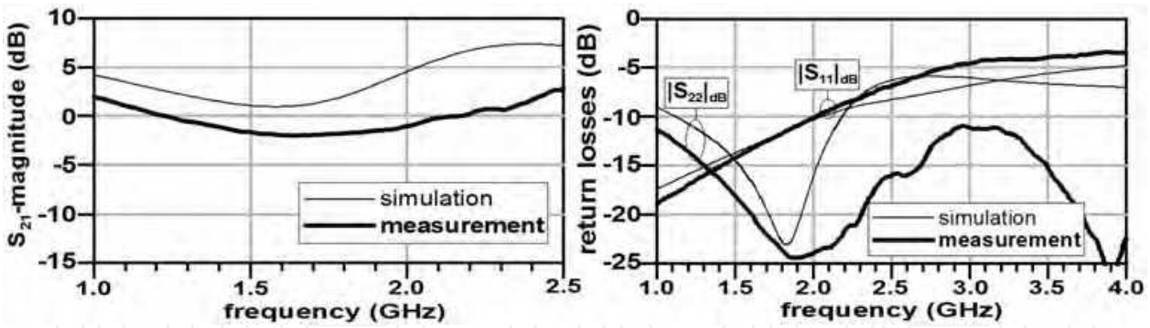


**(b)** **(c)**

Fig. 15. Comparisons of simulation- and measurement-results about $S_{21}$-magnitudes (b) and return losses (c).

These results are particularly encouraging and validate both the principle and the design process; and moreover, the PS performances may be further improved as illustrated in the following section.

***(c) Simulations and sensitivity analysis of a two-stage broadband NGD PS***: To enlarge the bandwidth of constant phase while keeping a significant gain, the two-stage prototype schematized in Fig. 16(a) was designed and simulated. As previously, it relies on the use of EC-2612 FETs biased via passive networks. The electromagnetic and schematic co-simulations with *Momentum/ADS™* were run on considering the layout presented in Fig. 16(b). The results of simulation, i.e. S-parameter magnitudes, the transmission phase and the group delay are displayed in Figs. 17(a) and (b) together with the results of a 30-trial Monte Carlo sensitivity analysis carried out to gain insight into the impact of the component tolerances on the circuit responses. Indeed, the parameters, $R$, $L$ and $C$, of the resonant networks and the transmission line lengths, $d$, were subjected to random variations of ±5% around their nominal values according to the Gaussian statistical distribution.

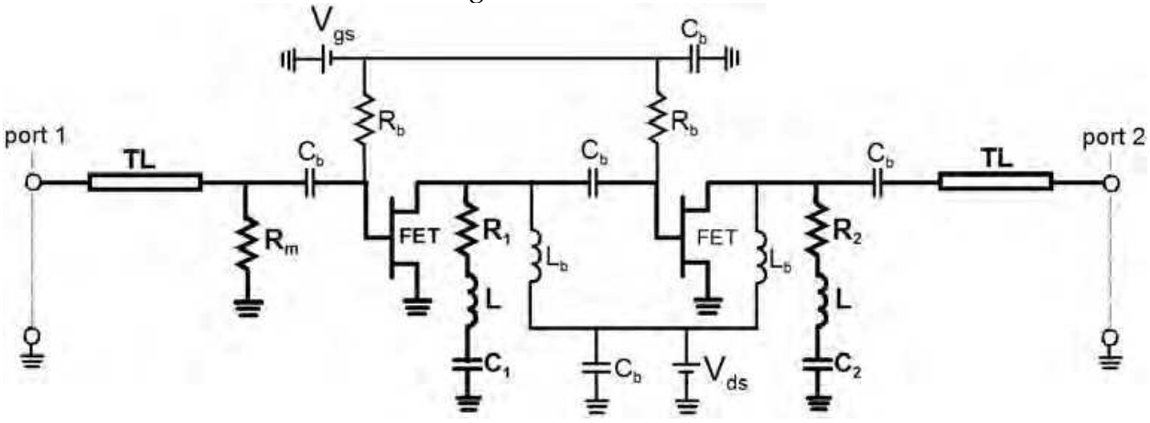


Fig. 16(a). Schematic of the simulated PS with a two-stage NGD circuit (EC-2612 FETs biased at $V_{gs}$ = -0.1 V, $V_{ds}$ = 3 V): $R_i$ = 62 Ω, $R_o$ = 120 Ω, $R_1$ = 43 Ω, $R_2$ = 75 Ω, $L$ = 2.2 nH, $C_1$ = 3.3 pF, $C_2$ = 1 pF, $C_b$ = 1 µF, $L_b$ = 330 nH, $R_b$ = 1 kΩ and $TL$ ($w$ = 952 µm, $d$ = 4.80 mm) printed on an FR4-substrate ($\varepsilon_r$ = 4.3/$h$ = 508 µm).

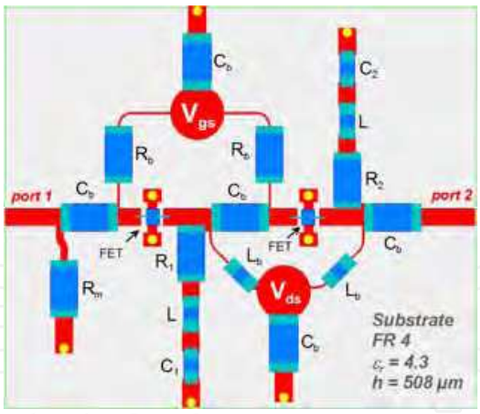


Fig. 16(b). Layout of the simulated NGD PS.

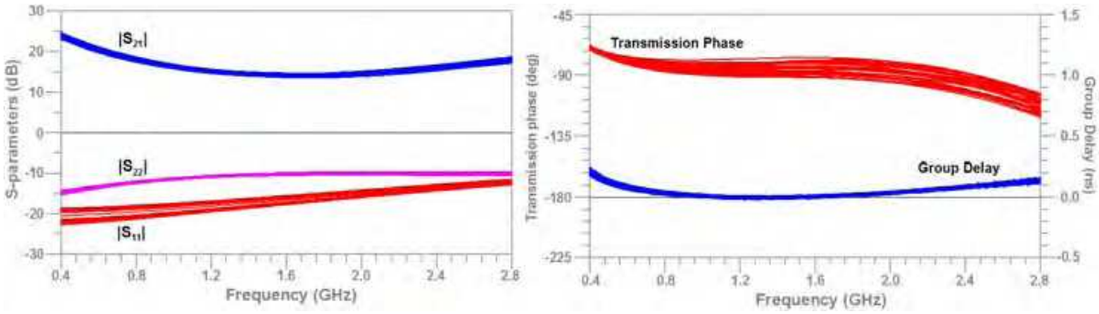


**(a)** **(b)**

Fig. 17(a). S-parameters magnitudes and (b) transmission phase and group delay with a Monte Carlo analysis as a function of *R*, *L*, *C* and *d*.

Let us first analyze the results of simulations for the nominal values: the -90°±10° constant phase extends from 0.6 GHz to 2.6 GHz (125% in relative). In this band, the gain is kept between 12 and 18 dB, the return losses are better than 10 dB and the group delay remains below 100 ps. The Monte-Carlo analysis shows that the S-parameters, $S_{11}$, $S_{21}$ and $S_{22}$, are within envelop limits with absolute differences less than 3 dB. Input- and output-matchings and gain flatness are kept. This confirms the relevance of cascading different NGD cells to widen the PS operating bandwidth. In a nutshell, this prototype of NGD PS is not sensitive to a variation of 5% on the passive element values and the transmission phase flatness is kept. One should note that a different trade-off could allow a slight increase of the constant phase bandwidth together with a decrease of the gain.
It is worth underlining that getting phase values between -180° and 0° is easier (smaller line) with an even number of cells; and between 0° and 180 with an odd number.

***(d) Potential applications of the under study NGD PS***: Compared to most of the PS available in the literature, this new PS configuration presents the following advantages:

- a constant transmission phase, which mathematically corresponds to a zero group delay, and generating in practice, a smaller value than that of a passive circuit of equivalent length,
- a possibility of implementation in very compact size,
- a faculty to achieve a broad operating bandwidth of constant phase,

- an easy way to achieve loss compensation or even an amplification thanks to the active circuit characteristics,
- the FET non-reciprocity entails a good isolation but this may be a drawback for certain applications,
- and the proposed topology provides a constant transmission phase and not a constant phase shift between the input and the output or between two outputs as it is often the case with many microwave PS.

These benefits lead us to envisage applications in electronic systems and notably the following ones in the telecommunication areas:

- integration in broadcasting systems such as active phased array antenna, as introduced in many papers (Wang et al., 1996 or Ko et al., 2003 for mobile satellite broadcasting),
- a good candidate for the improvement of modulator/demodulator functions in analog/digital communication systems (Phelan, 1975) such as PSK (phase shift keying), including BPSK (binary PSK), QPSK (Quadrature PSK), and MPSK (M-ary PSK, N bits),
- owing the faculty to provide gain, this NGD PS has an opportunity to operate as multifunction device (loss compensation, constant phase, delay reduction),
- integration in front-end RF architectures, for the synchronization of multipath systems,
- and thanks to the possibility of achieving flat or linear phase value at any levels, this PS is also promising to be useful in particular function such as frequency convertor, balun (Ravelo et al., 2007c), PLL, ...

In this optic of applications, a developed study on the design of a balun using the presented frequency-independent PS is proposed in the next subsection.

### 3.3 Design of a broadband active balun

The proposed three-port balun architecture is described in Fig. 18 (Ravelo et al., 2007c, 2008b). It presents an input, $v_{in}$ (port 1) and outputs, $v_{out}^-$ (port 2) and $v_{out}^+$ (port 3). We recall that by definition, a balun is a three-port device with the same amplitude and opposite phases at the two output ports:

$$\left|v_{out}^{+}\right| = \left|v_{out}^{-}\right|, \tag{38}$$

$$\left|\varphi_{v_{out}^{+}} - \varphi_{v_{out}^{-}}\right| = 180° . \tag{39}$$

Similar to many multi-port microwave devices, it should be associated with good return losses and isolation between the output ports.

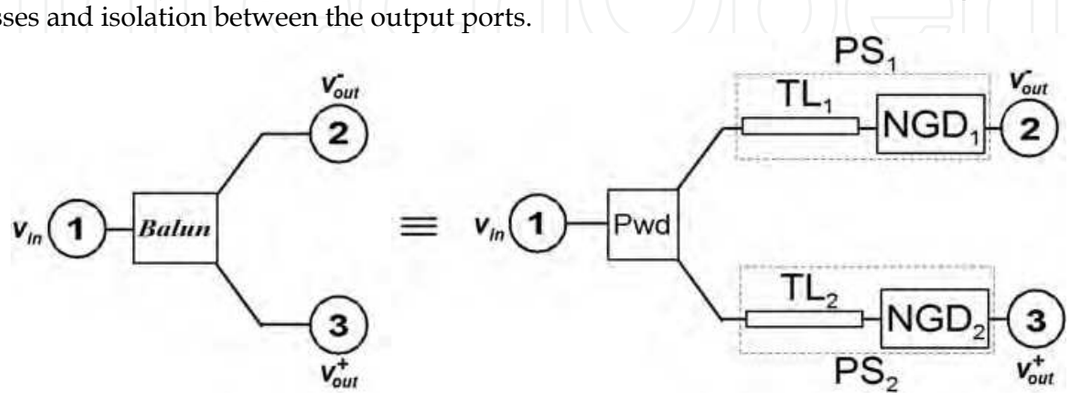


Fig. 18. Proposed architecture of balun with NGD active circuits (*Pwd*: Power divider).

To achieve the above specified functions, we use a power divider, *Pwd* in cascade with an NGD PS (a classical transmission line, TL, cascaded with an NGD circuit) in each of its output branches. The power divider ensures an equal power split. Then, to get the opposite phases at the output of the balun, the first branch exhibits, for a specified frequency band, a phase shift of -270° and the second one -90°. Here, in each branch of the splitter, a transmission line of negative phase slope is associated with an NGD active circuit of positive phase slope in order to finally get the desired constant phase value over a broadband defined between two frequencies, *f*1 and *f*2 for both outputs.Fig. 19 shows the schematic of the designed balun with two-stage of the NGD cells. In most of the cases (Antoniades & Eleftheriades, 2005; Lee et al., 2005), Wilkinson dividers are used, but they may restrict the operating bandwidth. In order to operate over a broad bandwidth, a 6 dB resistive splitter composed of a tree of identical resistors equal to $Z_0/3$ is used.

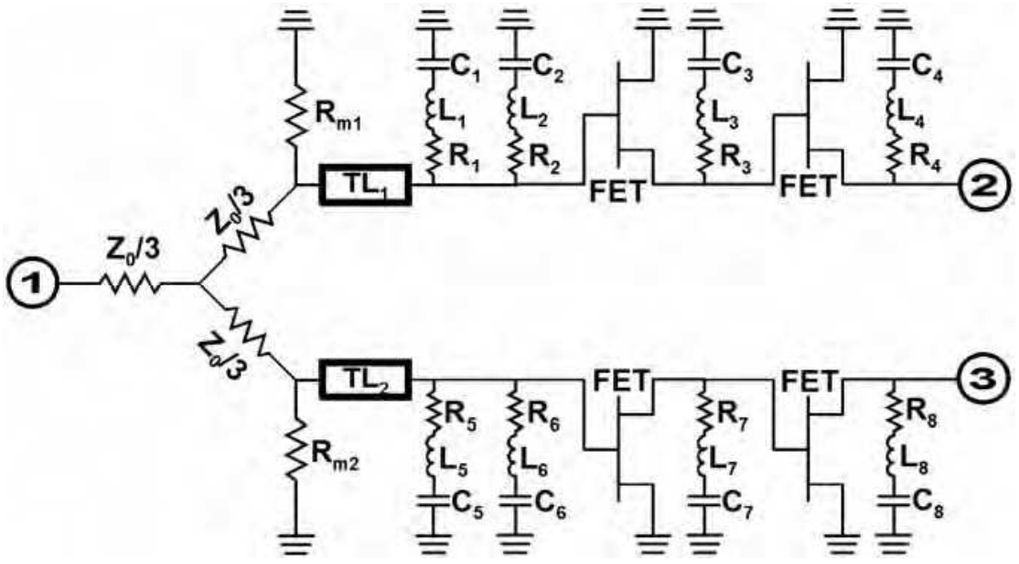


Fig. 19. Schematic of the simulated NGD active balun: $Z_0$ = 50 Ω, $R_1$ = 83 Ω, $R_2$ = 120 Ω, $R_3$ = 22 Ω, $R_4$ = 42 Ω, $R_5$ = 40 Ω, $R_6$ = 43 Ω, $R_7$ = 12 Ω, $R_8$ = 36 Ω, $R_{m1}$ = 120 Ω, $R_{m2}$ = 150 Ω, $L_1$ = 1 nH, $L_2$ = 320 pH, $L_3$ = 270 pH, $L_4$ = 531 pH, $L_5$ = 3.3 nH, $L_6$ = 6.5 nH, $L_7$ = 1.3 nH, $L_8$ = 3 nH, $C_1$ = 2.8 pF, $C_2$ = 2.6 pF, $C_3$ = $C_4$ = 2.4 pF, $C_5$ = 0.6 pF, $C_6$ = 0.1 pF, $C_7$ = 0.7 pF, $C_8$ = 0.6 pF, $TL_1$ ($d_1$ = 4.49 mm, $Z_{c1}$ = 50 Ω), and $TL_2$ ($d_2$ = 24.89 mm, $Z_{c2}$ = 50 Ω) printed on a RF35 substrate ($\varepsilon_r$ = 3.5, $h$ = 508 μm), FETs: EC-2612 biased at $V_{gs}$ = -0.1 V, $V_{ds}$ = 3 V.

The transmission lines $TL_i$ ($i$ = {1, 2}) are defined by their lengths, $d_i$, and their characteristic impedances, $Zc_i$ which are set at $Z_0$. $R_{m1}$ and $R_{m2}$ allow the matching between the splitter outputs and the input accesses. It is worth pointing out that, in order to achieve a constant phase value with a difference of 180°, $d_2$ is set longer than $d_1$. As illustrated in Fig. 20(a), the top branch ($TL_1$ and $NGD_1$) shows a nearly flat phase value of -90°±10° whereas that of the bottom one ($TL_2$ and $NGD_2$) is -270°±10° from 3.0 to 6.0 GHz. Figs. 20(a) and 20(b) show that the differential phase output is 180°±9°, and the insertion losses, $|S_{21}|_{dB}$ and $|S_{31}|_{dB}$, are greater than 2.4 dB. Thanks to the non-reciprocity of the employed FET, the isolation levels are better than -59 dB between all ports. In addition, the return losses $|S_{11}|_{dB}$ and $|S_{22}|_{dB}$ are better than 11 dB from 3.0 to 6.0 GHz, and the output return loss $|S_{33}|$dB is kept over

9 dB. Finally, the differential flatness, $||S_{31}|_{dB} - |S_{21}|_{dB}|$, is less than 1.1 dB from 3.5 to 6.0 GHz.

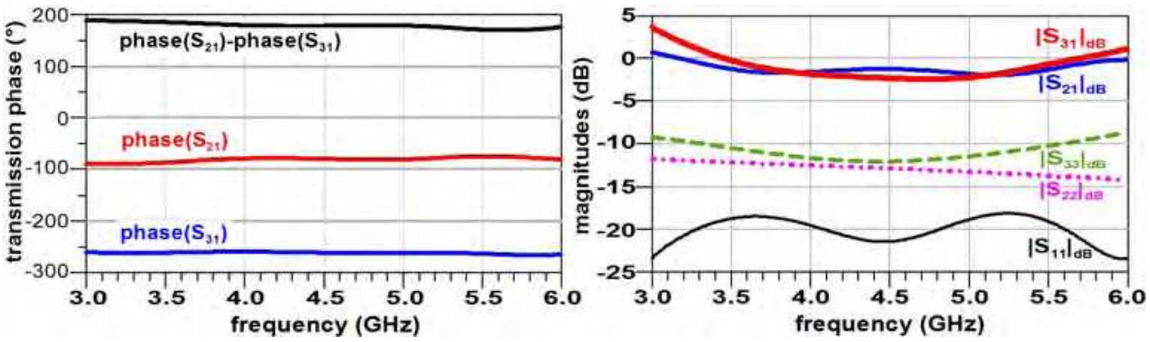


Fig. 20. Phases (a) and magnitudes (b) of the balun simulated S-parameters.

Table 1 summarizes the performances of the understudied balun shown in Fig. 19. More precisely, it deals with $S_{21}$- and $S_{31}$-magnitude and phase variations through the two output branches from 3.5 GHz to 5.5 GHz. We remark that they present magnitude and phase flatnesses respectively lower than 2.2 dB and 5°.

| **Insertion loss** | **Magnitude (dB)** | | **Phase (deg.)** | |
|---|---|---|---|---|
| | **Min.** | **Max.** | **Min.** | **Max.** |
| $S_{21}$ | -1.94 | -1.24 | -87.50 | -79.00 |
| $S_{31}$ | -2.40 | -0.24 | -263.50 | -260.00 |

Table 1. Simulated balun: phase and magnitude variations from 3.5 GHz to 5.5 GHz.

For such an active multi-port device, the stability must be ensured at every frequency. As previously, this circuit stability analysis was made by carefully verifying that the magnitude of the input and output reflexion coefficients of each transistor was kept below one up to 10 GHz.

On the other hand, in order to conclude about the noise factor of the balun under study, we intend to characterize a balun prototype through experiments carried out in frequency- and time-domains. These measurements should allow us to quantify the noise contribution. Nevertheless, it was verified by time-domain measurements (Fig. 7(a)) that the noise effect is not favoured by the NGD effect. Nevertheless, an increase of a possible noise contribution can be avoided by acting on the positions of the RLC-resonant network and of the transistors of the NGD circuit. Then, a trade-off with the matching level should be set.

The main assets of this compact broadband balun are its very low delay value, the possibility of loss compensation and its good isolation compared to most of the baluns described in the literature (Van Raay & Kompa, 2000; Kuylenstierna & Linner, 2004; Viallon et al., 2005; Antoniades & Eleftheriades, 2005; Lee et al., 2005).

## 4. Conclusion and future works

A simple topology of an NGD active circuit consisting in a FET terminated by a shunt RLC-resonant network and dedicated to the microwave signals was proposed and extensively studied. To our knowledge, this experimental demonstration in the time domain of the ability of a circuit to exhibit simultaneously gain and NGD in microwave domain is the first one available in the literature. By injecting in the NGD circuit a sufficiently smoothed input short-pulse modulating a sine carrier, we showed that the output has an envelop peak in advance compared to the input one. Of course, this phenomenon is not in contradiction with the causality principle. It is also worth emphasizing that the circuit under test meets all of the criteria required for classical active microwave devices, i.e. gain, matching and stability. As predicted by theory (Ravelo et al., 2007a, 2007b, 2007c and 2008a), for a prototype implemented in planar technology, measurements showed that, in the time-domain, the pulse peak advance was about -2 ns or 24% of the $1/e$-input pulse half-width with no attenuation. It is also worth noting that this experiment confirmed that the occurrence of time-domain advance induced by the NGD active circuit was not suppressed by the input noise contribution.

Moreover, thanks to the $S_{21}$-magnitude form, the NGD circuit under test demonstrated its ability to exhibit a pulse compression phenomenon together with a possibility of amplification. Then, it should be worth using the presented NGD active topology to compensate for dispersion effects and especially to reduce the intersymbol interference (ISI) in certain telecommunication channels.

As a potential application of this NGD circuit, we proposed a new principle of frequency-independent phase shifter. Cascading a classical transmission line with this NGD circuit allowed us to get a constant phase value. The efficiency of this principle was demonstrated by measurement. Indeed, a constant phase value of 90°±5° was obtained within a 76% relative frequency band centred at about 1.5 GHz. The impacts of the PS parameter variations were described and a sensitivity analysis was performed and discussed. The main benefits of this NGD active PS are its compactness and also the facility to generate very low group delay, and the broad band characteristics. Besides, a two-stage NGD PS was also designed; the simulation results showed a bandwidth enhancement of the constant phase up to 125% (-90°±10°). Some fields of applications such as the design of a broadband active balun for RF front end architectures are discussed.

As ongoing researches, design of reconfigurable devices dedicated to telecommunication applications is planned. Future investigations will be devoted to the design of NGD devices able to operate at higher frequencies through the use of distributed elements. In this prospect, implementation of MMIC devices based on distributed elements is envisaged.

## 5. References

Antoniades, M. A. & Eleftheriades, G. V. (2005). A broadband Wilkinson balun using microstrip metamaterial lines, *IEEE Ant. Wireless Propagation Lett.*, Vol. 4, Issue 1, pp. 209-212.

Arbore, M. A. (1997). Engineerable compression of ultrashort pulses by use of second-harmonic generation in chirped-period-poled lithium niobate, *Opt. Lett.*, Vol. 22, No. 17, pp. 1341-1343.

Baum, C. E. (2006). Coupling ports in waveguide cavities for multiplying fields in pulse-compression schemes, *Circuit and Electromagnetic System Design Note 52*.

Broomfield, C. D. & Everard, J. K. A. (2000). Broadband negative group delay networks for compensation of oscillators, filters and communication systems, *Electron. Lett.*, Vol. 23, pp. 1931-1933.

Burt, G.; Samsonov, S. V.; Phelps, A. D. R.; Bratman, V. L.; Ronald, K.; Denisov, G. G.; He, W.; Young, A. R.; Cross, A. W. & Konoplev, I. V. (2005). Microwave pulse compression using a helically corrugated waveguide, *IEEE Trans. On Plasma Science*, Vol. 33, No. 2, pp. 661-667.

Cao, H.; Dogariu A.; & Wang, L. J. (2003). Negative group delay and pulse compression in superluminal pulse propagation, *IEEE J. Sel. Top. Quantum Electron.,* Vol. 9, No.1, pp. 52-58.

Chiao, R. Y.; Bolda, E. L.; Bowie, J.; Boyce, J. & Mitchell, M. W. (1996). Superluminality and amplifiers, *Prog. Crystal Growth Charact. Mat. 33*, pp. 319-325.

Chu, S. & Wong, S. (1982). Linear pulse propagation in an absorbing medium, *Phys. Rev. Lett.*, Vol. 48, pp. 738-741.

Eleftheriades, G. V.; Siddiqui, O. & Iyer, A. K. (2003). Transmission line for negative index media and associated implementations without excess resonators, *IEEE MWC Lett.*, Vol. 13, No. 2, pp. 51-53.

Gaponov-Grekhov, A. V. & Granatstein, V. L. (1994). Applications of high-power microwaves, Ed. Hardcover, Pages No. 364, Artech House, ISBN: 0-89006-699-x, Boston, MA.

Garrett, C. G. B. & McGumber, D. E. (1970). Propagation of a gaussian light pulse through an anomalous dispersion medium, Phys. Rev. A, Vol. 1, pp. 305-313.

Kitano, M.; Nakanishi, T. & Sugiyama, K. (2003). Negative group delay and superluminal propagation: an electronic circuit approach, *IEEE J. Sel. Top. Quantum Electron.*, Vol. 9, No. 1, pp. 43-51.

Ko, Y. J.; Park, J. Y. & Bu, J. U. (2003). Integrated RF MEMS phase shifters with constant phase shift, *IEEE MTT-S Symp. Dig.*, Philadelphia, pp. 1489-1492, June 2003.

Kuylenstierna, D. & Linner, P. (2004). Design of broad-band lumped-element baluns with inherent impedance transformation, *IEEE MTT*, Vol. 52, No. 12, pp. 2739-2745.

Kuzikov, S. V.; Danilov, Y. Y.; Denisov, G. G.; Shegokov D. Y. & Vikharev, A. A. (2004). Multi-mode sled-II pulse compressors, *Proc. LINAC2004*, Lübek Germany, THP28, pp. 660-662.

Lee, S.; Lim, J-S.; Yang H-S. & Nam, S. (2005). A novel design of balun using left handed transmission line, *Proceedings of ISAP2005*, Seoul, Korea.

Li, P.; Chen, X.; Chen, Y. & Xia, Y. (2005). Pulse compression during second-harmonic generation in engineered aperiodic quasi-phase-matching gratings, *Optics Express*, Vol. 13, No. 18, pp. 6807-6814.

Lucyszyn, S.; Robertson, I. D. & Aghvami, A. H. (1993). Negative group delay synthesiser, *Electron. Lett.*, Vol. 29, pp. 798-800.

Mitchell, M. W. & Chiao, R. Y. (1997). Negative group delay and 'fronts' in a causal systems: an experiment with very low frequency bandpass amplifiers, *Phys. Lett. A*, Vol. 230, pp. 133-138.

Mitchell, M. W. & Chiao, R. Y. (1998). Causality and negative group delays in a simple bandpass amplifier, *Am. J. Phys. 66*, pp. 14-19.

Munday, J. N. & Henderson, R. H. (2004). Superluminal time advance of a complex audio signal, *Appl. Phys. Lett.*, Vol. 85, pp. 503-504.

Nakanishi, T.; Sugiyama, K. & Kitano, M. (2002). Demonstration of negative group delays in a simple electronic circuit, *Am. J. Phys.*, Vol. 70, Issue 11, pp. 1117-1121.

Phelan, H. R. (1975). Dual polarization spiral antenna, *U.S. patent No. 3,906,514*, Sep. 16.

Ravelo, B. (Dec. 2008). Negative group delay active devices: theory, experimental validations and applications, *Ph. D. thesis* (*in French*), Lab-STICC, UMR CNRS 3192, UEB, University of Brest, France.

Ravelo, B.; Pérennec, A.; Le Roy, M. & Boucher, Y. (2007a). Active microwave circuit with negative group delay, *IEEE MWC Lett.*, Vol. 17, Issue 12, pp. 861-863.

Ravelo, B.; Pérennec, A. & Le Roy, M. (2007b). Synthesis of broadband negative group delay active circuits, *IEEE MTT-S Symp. Dig.*, *Honolulu (Hawaii)*, pp. 2177-2180.

Ravelo, B.; Pérennec, A. & Le Roy, M. (2007c). Broadband balun using active negative group delay circuit, *Proc. of the 37th EuMC*, Munich, Germany, 8-12 Oct. 2007, pp. 466-469.

Ravelo, B.; Pérennec, A. & Le Roy, M. (2008a). Negative group delay active topologies respectively dedicated to microwave frequencies and baseband signals, *Journal of the EuMA*, Vol. 4, pp. 124-130.

Ravelo, B.; Pérennec, A. & Le Roy, M. (2008b). Application of negative group delay active circuits to the design of broadband and constant phase shifters, *Microwave And Optical Technology Lett.*, Vol. 50, No. 12, pp. 3078-3080.

Siddiqui, O. F.; Erickson, S. J.; Eleftheriades G. V. & Mojahedi, M. (2004). Time-domain measurement of negative group delay in negative-refractive-index transmission-line metamaterials, *IEEE Trans. MTT*, Vol. 52, No. 5, pp. 1449-1454.

Thumm, M. K. & Kasparek, W. (2002). Passive high-power microwave components, *IEEE Trans. Plasma Sci.*, Vol. 30, No. 3, pp. 755-786.

Van Raay, F. & Kompa, G. (2000). Design and stability test of a 2-40 GHz frequency doubler with active balun, *IEEE MTT-S Symp. Dig.*, Honolulu (Hawaii), Vol. 3, Boston, MA, pp. 1573-1576.

Viallon, C.; Venturin, D.; Graffeuil, J. & Parra, T. (2005). Design of an original K-band active balun with improved broadband balanced behavior, *IEEE MWC Lett.*, Vol. 15, No.4, pp. 280-282.

Wang, C. & Yao, J. (2008a). Photonic generation of chirped millimeter-wave pulses based on nonlinear frequency-to-time mapping in a nonlinearly chirped fiber Bragg grating, *IEEE Tran. MTT*, Vol. 56, No. 2, pp. 542-553.

Wang, C. & Yao, J. (2008b). Photonic generation of chirped microwave pulses using superimposed chirped fiber Bragg gratings, *IEEE Photon. Technol. Lett.*, Vol. 20, No. 11, pp. 882-884.

Wang, L. J.; Kuzmich, A. & Dogariu, A. (2000). Gain-assisted superluminal light propagation, *Nature 406*, pp. 277-279.

Wang, J. J. H.; Tillery, J. K.; Thompson, G. T.; Bohannan, K. E.; Najafabadi, R. M. & Acre, M. A. (1996). A multioctave-band photonically-controlled, low-profile, structurally-embedded phased array with integrated frequency independent phase-shifter, *IEEE Int. Symp. on Phased Array Syst. Technol.*, pp. 68-73, Oct. 15-18, 1996, Boston, MA.

Zeitouny, A.; Stepanov, S.; Levinson, O. & Horowitz, M. (2005). Optical generation of linearly chirped microwave pulses using fiber Bragg gratings, *IEEE Photon. Technol. Lett.*, Vol. 17, No. 3, pp. 660-662.


**Microwave and Millimeter Wave Technologies Modern UWB antennas and equipment**

Edited by Igor Mini

ISBN 978-953-7619-67-1
Hard cover, 488 pages
**Publisher** InTech
**Published online** 01, March, 2010
**Published in print edition** March, 2010

**How to reference**

In order to correctly reference this scholarly work, feel free to copy and paste the following:

Blaise Ravelo, Andre Perennec and Marc Le Roy (2010). Study and Application of Microwave Active Circuits with Negative Group Delay, Microwave and Millimeter Wave Technologies Modern UWB antennas and equipment, Igor Mini (Ed.), ISBN: 978-953-7619-67-1, InTech, Available from: http://www.intechopen.com/books/microwave-and-millimeter-wave-technologies-modern-uwb-antennas-and-equipment/study-and-application-of-microwave-active-circuits-with-negative-group-delay



**InTech Europe**
University Campus STeP Ri
Slavka Krautzeka 83/A
51000 Rijeka, Croatia
Phone: +385 (51) 770 447
Fax: +385 (51) 686 166
www.intechopen.com

**InTech China**
Unit 405, Office Block, Hotel Equatorial Shanghai
No.65, Yan An Road (West), Shanghai, 200040, China
中国上海市延安西路65号上海国际贵都大饭店办公楼405单元
Phone: +86-21-62489820
Fax: +86-21-62489821

IntechOpen